Chapter 5

Synthesis and Characterisation of $Sr_2Mn_{1-x}Sn_xO_4$

Part of this chapter is published as 'Gurudeo Nirala, Dharmendra Yadav, Tarun Katheriya & Shail Upadhyay; Temperature dependent negative permittivity in solid solutions $Sr_2Mn_{1-x}Sn_xO_4$ (x = 0, 0.3, 0.5); *J. Eur. Ceram. Soc.* **42**, 453–461 (2022).'

5.1 Introduction

In recent years, materials with negative permittivity have attracted a great deal of attention due to their potential applications in electromagnetic shielding [119], capacitors [222], transistors [223], antennas [224], inductor design, and other electronic devices. A negative dielectric constant (NDC) is often observed in metals below their plasma frequency due to the plasmonic oscillation of free electrons [103,249]. Negative dielectric properties of metals led to the investigation and design of metamaterials, in which tailorable negative permittivity depends on the geometrical dimensions and configurations of the metal building blocks [102,118,225]. An extensive literature survey has demonstrated that negative permittivity can also be realized in composites with functional metal fillers randomly dispersed in insulator matrix [109,112,250,251]. The negative dielectric permittivity of composites depends mainly on the critical structures of conductor fillers in which the free charge carriers oscillate with the variation of the electric field [252–254]. Various ceramic matrix composites (CMCs) and polymer matrix composites (PMCs) have been synthesized designed and synthesized to obtain tailorable negative dielectric properties in specified frequency ranges [136,137,146,229,255,256].

Metamaterials and composites can be regarded as diluted metals to realize tailorable negative permittivity properties by controlling the average electrons concentration. From the perspective of the relationships between negative permittivity and electrons density, it is necessary to realize desirable negative dielectric behavior in single-phase materials. For the films or coating purposes single-phase materials are more reliable as compared to composites and metamaterials. Perovskite manganites $AMnO_3$ (A = Pr, La) systems have also exhibited negative permittivity behavior which is attributed to their metal-like characteristics [257,258] [259,260]. Recently, negative permittivity was realized in the single-phase ceramic oxides SnO_2 and In_2O_3 through donor doping [236,261].

The synthesis of Sr_2MnO_4 is a challenging task by normal solid-state reaction method [165,238]. However, Sr_2MnO_4 powder can be synthesized by quenching in the air from 1500°C to room temperature [238]. Further, partial replacement of Sr by La (concentration ≥ 0.3 mole %) can produce single phases via a normal solid-state ceramic route. The studied compositions of La doped Sr_2MnO_4 in last chapter has shown the negative permittivity behaviour at all measuring temperature. Since La is a rare element. It is advisable to find some another dopant, whose partial replacement should produce single phase Sr_2MnO_4 via a normal solid-state ceramic route and may show negative permittivity. The Sr_2MnO_4 and Sr_2SnO_4 are isostructural, also isostructural to the K_2NiF_4, and both crystallized with a tetragonal unit cell in the same space group I4/mmm [238,262]. The Sr_2SnO_4 can be synthesisable by normal solid-state ceramic route at 1200 °C [262], which is lower than the Sr_2MnO_4 sintering temperature [238]. Therefore, Sr_2SnO_4 can act as a nucleation seed due to their isostructural nature and lower synthesis temperature. Thereby, the partial replacement of Mn by Sn or solid solution of $Sr2MnO_4$ and Sr_2SnO_4 may produce single phases via a normal solid-state ceramic route. With this intension, in this chapter, I have tried to study the effect of Sn doping at the Mn on phase formation and microstructure, by synthesizing four compositions (with x = 0.30, 0.50, 0.70, 1.0) of $Sr_2Mn_{1-x}Sn_xO_4$ system, and further dielectric properties by synthesizing compositions were studied. To the best of my knowledge, no report is available in the literature on the temperature and frequency-dependent dielectric properties of Sr_2MnO_4 and Sn substituted Sr_2MnO_4. In this work, the dielectric properties of $Sr_2Mn_{1-x}Sn_xO_4$ system were investigated by measuring real (Z') and imaginary (Z") components of the complex impedance, Z*, in the temperature range 30-600 °C and in the frequency range 20 Hz - 2 MHz.

5.2 Experimental

In this work, a conventional solid-state reaction route has been used to prepare two compositions (x = 0.3, 0.5, 0.7, 1.0) of the system $Sr_2Mn_{1-x}Sn_xO_4$. The starting compounds $SrCO_3$ (Sigma-Aldrich, purity ≥ 99.9%), MnO_2 (Sigma-Aldrich, purity ≥ 99%), and SnO_2 (Alfa Aesar, purity ≥ 99.9%) were taken in the stoichiometric ratio and mixed in a ball mill (PM-200, Retsch, Germany) for 8 hours in acetone medium. These mixtures were then calcined for 12 hours at 1200 ^oC in a high-temperature furnace (HTRH-70/150, Carbolite Gero, UK). Calcined powders were ground in an agate mortar and recalcined for 12 hours at 1500 ^oC. For microstructure, dielectric/electrical measurements, and XPS, the pellets with a diameter of 7-8 mm and a thickness of 2-3 mm were prepared using a hydraulic press by applying the pressure of 5 kN. Prepared green pellets were sintered at 1500 ^oC for 12 hours and cooled to room temperature with 4 ^oC/min. The prepared pellet of undoped Sr_2MnO_4 used in the study of chapter 3 is used hare for studying the dielectric property of pure Sr_2MnO_4. For convenience, in succeeding sections these samples have been addressed by code names such as SMS0, SMS3, SMS5, SMS7 and SMS10 for Sr_2MnO_4, $Sr_2Mn_{0.7}Sn_{0.3}O_4$, $Sr_2Mn_{0.5}Sn_{0.5}O_4$, $Sr_2Mn_{0.3}Sn_{0.7}O_4$ and Sr_2SnO_4, respectively.

The X-ray diffraction (XRD) pattern of the sintered pellets was recorded at room temperature using a diffractometer (Rigaku Miniflex II Desktop, Japan). The morphological fingerprints of the fractured surfaces of the sintered pellets were recorded using a field emission Scanning Electron Microscope (Nova Nano SEM 450, USA). For dielectric/electrical properties measurements, circular surfaces of the sintered pellets were polished using emery paper of different grades and then coated with a thin and uniform layer of high-temperature silver paste. Real (Z') and imaginary (Z") parts of the impedance (Z) were measured as a function of the frequency (in the range of 20 Hz–2 MHz) and temperature (in the range of 30-

600 °C), using an inductance-capacitance-resistance (LCR) meter (Agilent E-4980, USA). To know the valence state of constituent elements Mn and Sn, present in the samples, the surfaces of the pellets were scorched and polished with the various grades of emery paper. Thereafter, the core spectra of these elements were obtained using an X-ray photoelectron spectrometer (Thermo Fisher Scientific K-Alpha, USA), operating at the high pressure of 5×10^{-11} Torr. The UV-visible-IR spectra of the samples were recorded using a UV-Visible-IR spectrophotometer (JASCO V-770, Japan) in the wavelength range of 300-1700 nm.

5.3 Results and Discussion

5.3.1 Phase and Crystal structure analysis

The X-ray diffraction (XRD) pattern of all the synthesized compositions of the system $Sr_2Mn_{1-x}Sn_xO_4$ was recorded and shown in Fig. 5.1(a). The XRD patterns were matched with the Crystallography Open Database (COD) for Sr_2MnO_4 (1008125). No distinct peaks corresponding to raw materials SrO, MnO_2, and SnO_2 or expected secondary phase $Sr_7Mn_4O_{15}$ were observed in synthesized compositions, which confirmed the formation of single-phase solid solutions. For comparisons, the XRD pattern of the sample with x=0.0 (SMS0) studied in chapter 3 is also shown in Fig. 5.1(a). A systematic shift of the peaks towards the lower angle side with increasing dopant (Sn) concentration (x) was observed. A magnified view of the shift of the peak corresponding to the plane (103) and (110) is shown in the same figure. The ionic radius of Sn^{4+} is 0.69 Å, larger than the ionic radius of Mn^{4+} (0.53 Å) in the same coordination number six [239]. Therefore, the observed peak shift is a signature of the replacement of Mn^{4+} ions by Sn^{4+} ions in the lattice of Sr_2MnO_4.

The structural parameters of the synthesized compositions were obtained with the help of Rietveld refinement using the FullProf Suite software package. The structural refinement was carried out by considering the tetragonal structure and space group I4/mmm. The

calculated XRD pattern obtained after the final refinement is shown in Fig. 5.1(b, c, d, e). A good matching between the experimentally recorded and calculated XRD patterns was seen. The obtained structural parameters are summarized in Table 5.1. The value of these parameters for the sample SMS0 (Sr_2MnO_4) is also shown in the table for comparison. The variation of the lattice parameters and the unit cell volume with dopant (Sn) concentration (x) is shown in Fig. 5.1(f). The lattice parameters (a and c), as well as the unit cell volume, have increased on increasing Sn concentration in the solid solution. The expansion in unit cell volume with increasing Sn concentration is consistent with the recorded XRD peak shift toward lower angles. The increase in Sr-O (1) and Mn/Sn- O (1) bond lengths on increasing dopant concentration (x) also confirms the same.

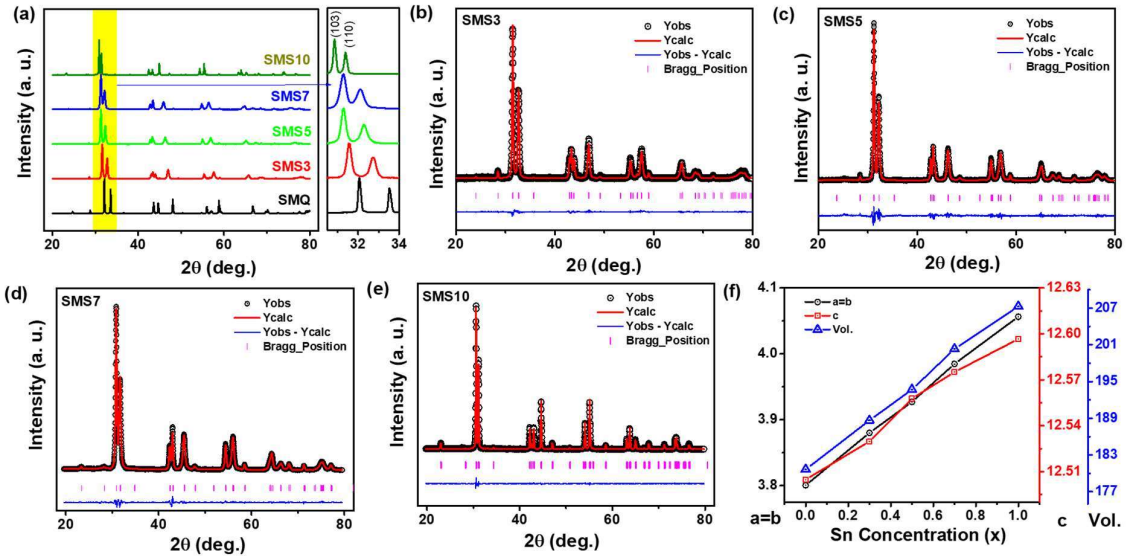

Figure 5.1. (a) Room temperature XRD pattern of the samples, (b, c, d e) Rietveld refined XRD pattern of the samples (f) Variation of lattice parameters with Sn Concentration (x).

To analyze the stability of prepared solid solutions, the value of the tolerance factor (t) and Global instability index (GII) has been calculated. In the case of layered perovskites, t estimates the compatibility of perovskite and rocksalt layer. While *GII* represents the instability of the structure and a larger *GII* indicates a less stable structure [240]. The equations for the calculation of the tolerance factor and Global instability index (*GII*) are given below:

$$t = \frac{r_{Sr} + r_O}{\sqrt{2} * ((1-x) \times r_{Mn} + x \times r_{Sn} + r_O)} \qquad (5.1)$$

where $r_{Sr}, r_{Mn}, r_{Sn}, r_O$ are the effective radii of Sr, Mn, Sn, O, respectively and x is the Sn concentration in the prepared samples. And,

$$GII = \frac{\sqrt{\sum_{i=1}^{N}\{\sum_j (S_{ij} - V_i)^2\}}}{N} \qquad (5.2)$$

where S_{ij} is the sum of the valence bonds around each ion and $V_i = \sum_j S_{ij}$. The value of S_{ij} is determined by the semi-empirical expression $S_{ij} = \exp[(R_o - R_{ij})/0.37]$, where R_o is a constant characteristic of the bond type. Calculated values of tolerance factor (t) and Global instability index (GII) are listed in Table 5.1. As Sn concentration (x) increases tolerance factor (t) decreases whereas the Global instability index (GII) increases. The Sr_2MnO_4 is stable only at temperatures higher than 1350 °C, below this temperature it decomposes in $Sr_7Mn_4O_{15}$ and SrO [165]. To stabilize Sr_2MnO_4 phase at lower temperatures approximately 30% of Mn ions should be present in Mn^{3+} state [73,241]. To achieve this goal, synthesis of Sr_2MnO_4 has been carried reducing atmospheres [241–244]. In our recent studies, we had been able to stabilize Sr_2MnO_4 at room temperature by quenching from high temperature (1500°C) to room temperature in the air [238]. Although t decreases and GII increases with increasing concentration of dopant (x), dopant Sn helps in stabilizing Sr_2MnO_4 phase at lower temperatures. Thus, Sn plays the same role as reducing atmospheres and quenching are playing in stabilizing Sr_2MnO_4 phase at lower temperatures. Here it is also important to mention that, the calculated values of t and GII of Sn substituted Sr_2MnO_4 are in the range of other reported A_2BO_4 compound [240,245,246].

Table 5.1. Structural parameters and reliability factors obtained by Rietveld refinement of the XRD patterns.

Sample Composition	Sr_2MnO_4	$Sr_2Mn_{0.7}Sn_{0.3}O_4$	$Sr_2Mn_{0.5}Sn_{0.5}O_4$	$Sr_2Mn_{0.3}Sn_{0.7}O_4$	Sr_2SnO_4
Sample Code	**SMS0**	**SMS3**	**SMS5**	**SMS7**	**SMS10**
a = b (Å)	3.795	3.880	3.927	3.984	4.056
c (Å)	12.500	12.530	12.558	12.615	12.596
Cell Volume ($Å^3$)	180.636	188.653	193.689	200.307	207.270
Sr (4e)	(0, 0, 0.357)	(0, 0, 0.355)	(0, 0, 0.354)	(0, 0, 0.354)	(0, 0, 0.354)
Mn/Sn (2a)	(0, 0, 0)	(0, 0, 0)	(0, 0, 0)	(0, 0, 0)	(0, 0, 0)
O (1) (4c)	(0, 0.5, 0)	(0, 0.5, 0)	(0, 0.5, 0)	(0, 0.5, 0)	(0, 0.5, 0)
O (2) (4e)	(0, 0, 0.161)	(0, 0, 0.161)	(0, 0, 0.158)	(0, 0, 0.163)	(0, 0, 0.163)
Mn/Sn-O (1)	1.897 Å	1.940 Å	1.963 Å	1.992 Å	2.028 Å
Mn/Sn-O (2)	2.018 Å	2.027 Å	1.985 Å	2.058 Å	2.053 Å
Sr-O (1)	2.607 Å	2.653 Å	2.680 Å	2.713 Å	2.744 Å
Sr-O (2)	2.693 Å	2.426 Å	2.468 Å	2.408 Å	2.395 Å
Mn(Sn)-O (1)/Mn(Sn)-O (2)	0.94	0.96	0.98	0.96	0.98
R_p	7.7	14.8	12.0	5.66	8.54
R_{wp}	4.8	10.8	12.3	6.36	9.30
R_{exp}	6.9	9.7	12.3	3.33	3.09
χ^2	2.01	1.99	1.96	2.65	2.04
t	0.993	0.969	0.953	0.938	0.917
GII	0.33	0.38	0.40	0.36	0.31

5.3.2 Microstructural characterization

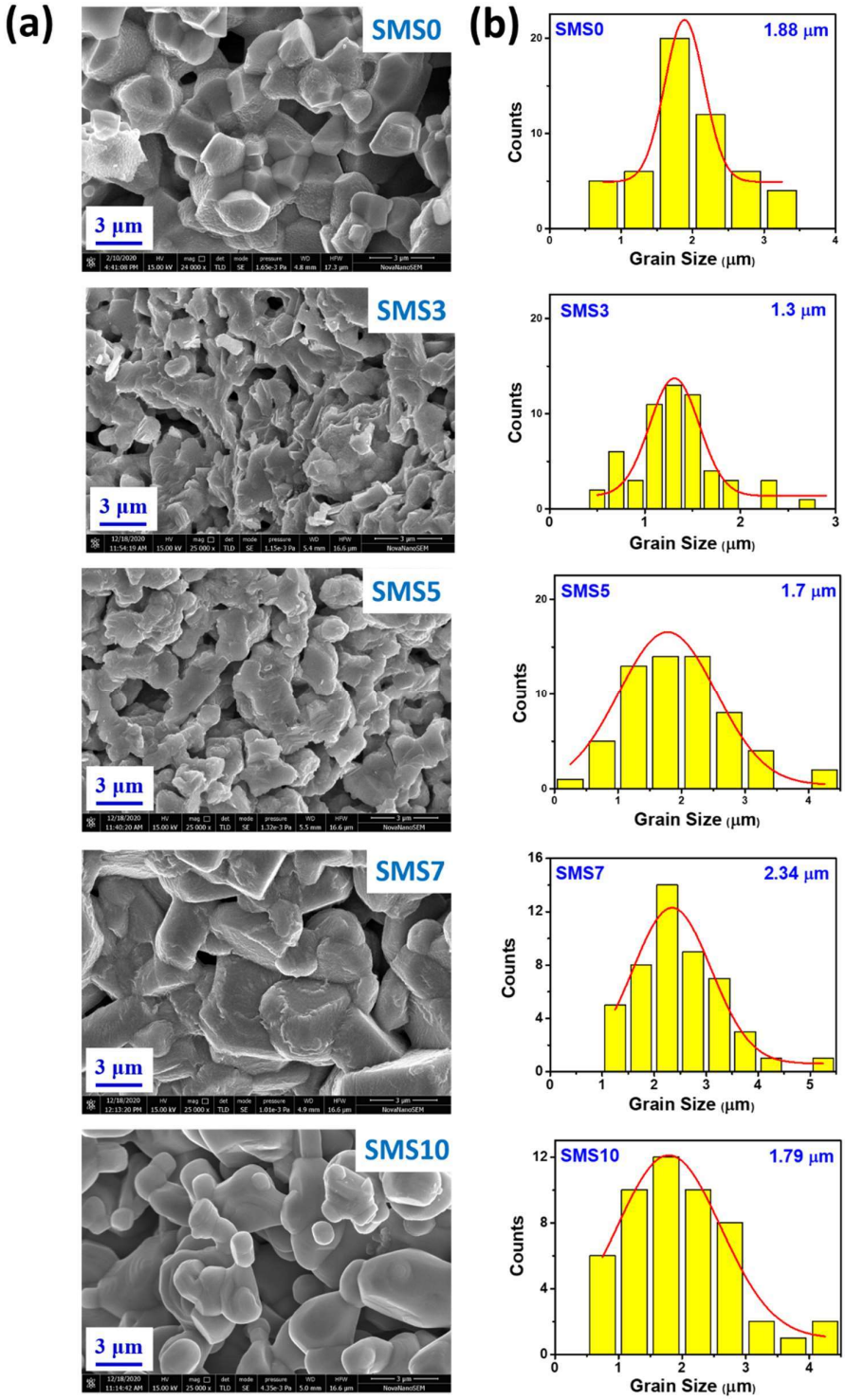

Figure 5.2. (a) SEM images of the fractured surfaces of the sintered pellets (b) Histograms showing the distribution of grain size in the samples.

For studying the effect of Sn substitution on morphology, a scanning electron microscopy (SEM) technique was employed. The recorded SEM images of the fractured surfaces of the sintered pellets are shown in Fig. 5.2(a). The micrographs corresponding to each composition are homogeneous, showing well-developed grains, separated by well-defined grain boundaries, a typical characteristic feature of a polycrystalline material. The observed morphology of the grains for the sample SMS3, SMS5, and SMS7 is different than that of the sample SMS0 and SMS10. In general, the morphology of the solid solutions highlights features of both the end members i.e., of Sr_2MnO_4 and Sr_2SnO_4 in this case. In the literature it is found that calcination temperature of Sr_2MnO_4 (> 1350 °C) is higher than calcination temperature (1200°C) for Sr_2SnO_4 [34,165]. Therefore, it is speculated that nuclei of Sr_2SnO_4 should have played the role of seeds for the grain growth, hence the observed morphologies of sample SMS3, SMS5 and SMS7 are different from SMS0. The observed morphologies of sample SMS3, SMS5 and SMS7 are also different from SMS10, since SMS10 sample is pure Sr_2SnO_4 and does not have contribution from Sr_2MnO_4. A histogram of the distribution of grain size for all the samples was obtained using the ImageJ software package. By fitting the Gaussian function to these histograms (Fig. 5.2(b)) average grain size for all the samples was calculated and written on their respective histogram. The average grain size is found to be smallest for the sample SMS3.

5.3.3 Negative Permittivity

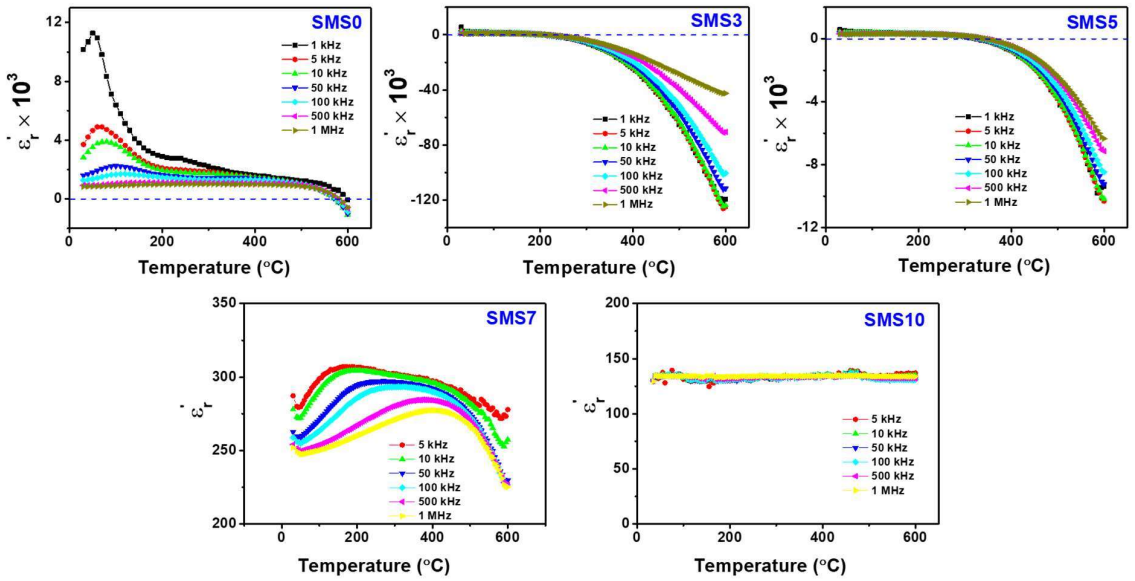

Figure 5.3. Temperature dependence of the real part of the relative permittivity at few representative frequencies.

The permittivity of the samples was calculated from measured impedance data, by the following equation:

$$\varepsilon_r^* = \frac{1}{i\omega C_0 Z^*} \qquad (5.3)$$

where, $\varepsilon_r^* (= \varepsilon_r' + i\varepsilon_r'')$ is complex relative permittivity, i is an imaginary unit ($i^2 = -1$), ω is the angular frequency of the applied signal, $C_0 = \varepsilon_0 A/d$, ε_0 = permittivity of free space (8.85×10^{-12} Fm^{-1}), A = electrode surface area, d = separation between the electrodes and $Z^* (= Z' + iZ'')$ is the complex impedance. The variation of the real component of the relative permittivity, ε_r' with the temperature at few representative frequencies is shown in Fig. 5.3. In the plot of the SMS0 and SMS7 a peak was observed. The height of the peak decreases and the position shifts toward higher temperatures with increasing frequency. These features are experimental evidence of the dielectric relaxation phenomenon in the sample. The dielectric relaxation peak in this sample may be due to the presence of oxygen vacancies or a variable

oxidation state of Mn. In the middle-temperature ranges (200-500 ^oC), weak dependencies of both frequency and temperature on permittivity were observed. The dielectric constant of sample SMS10 (Sr_2SnO_4) is remained constant irrespective of studied temperature and frequency range, is an example temperature and frequency stable dielectric material. In sample SMS0 above 500 ^oC, the permittivity begins to decrease and its values become negative above a particular temperature.

The ε_r' vs temperature plots for the samples SMS3 and SMS5 are similar, the permittivity remains almost constant and positive upto a particular temperature and starts decreasing on further increase of the temperature, becomes negative on further increase in the temperature. The temperature at which, ε_r' changes sign has referred as critical transition temperature (T_c). The value of T_c is different for different samples, 580 ^oC, 220 ^oC, and 350 ^oC, respectively for the samples SMS0, SMS3, and SMS5. Furthermore, it is noticed that T_c increases (10-20^oC) whereas the absolute value of ε_r' decreases with increasing frequency. The sample SMS7 and SMS10 show only positive dielectric constant in studied temperature and frequency range. As per the objective of this work, in the succeeding sections, experimental results of only SMS0, SMS3 and SMS5 samples have been described.

To get insight into the origin of negative dielectric constant, the variation of ε_r' with frequency at few selected temperatures is shown in Fig. 5.4. As mentioned above, the dielectric constant of all the samples remains positive up to critical temperature (T_c) and negative above this temperature. Therefore, the variation of ε_r' with frequency for the measured temperature range (30-600^oC) was divided into two groups, below T_c and above T_c. Fig. 5.4(a) shows the variation for the temperatures below T_c, while the variation temperatures above T_c are shown in Fig. 5.4(b). As can be seen in Fig. 5.4(a) ε_r' decrease with increasing frequency at all the temperatures. A sharp decrease in the values of ε_r' below 10 kHz is attributable to the interfacial

polarization. In addition, the decrease in the value at a fixed frequency with increasing temperature also supports the contribution of interfacial polarization in the synthesized samples. In polycrystalline materials, interfacial polarization arises due to differences in the electrical conductivity of the grains and grain boundaries. The reason for the difference in the conductivity of the grains and grain boundaries for the sample SMS0 has been discussed by us in detail [238]. In the plot of the sample SMS3 and SMS5, a decrease in values of ε_r' with increasing frequency was also seen, which is ascribed to the relaxation of space charge polarization. Fig. 5.4(b) shows the variation of ε_r' with frequency for the temperatures above T_c. In the frequency range 1 kHz to 2 MHz, values of ε_r' remain negative but absolute values decrease with increasing frequency.

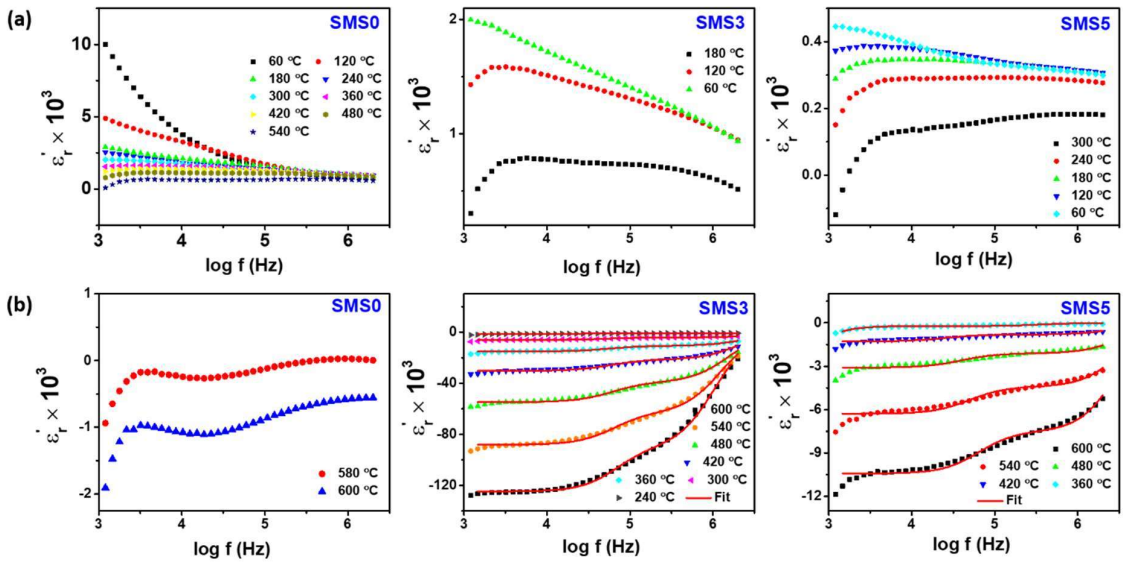

Figure 5.4. Variation of the real part of the relative permittivity with frequency at few selected temperatures.

In 1900 Drude proposed a model to explain the negative permittivity behavior of metals [108,153,229,234]. We tried to fit the Drude model to the experimental data points shown in Fig. 5.4(b) for the samples SMS3 and SMS5. It was observed that experimental data points are not in agreement with data generated according to the Drude model, the reason may be the

presence of both bound (localized) and free (delocalized) electrons in the samples. The Drude-Lorentz (DL) model has been employed by the researchers to explain the negative permittivity behavior of semiconductors possessing both localized (bound) and delocalized (free) charge carriers. According to this model, the real part of the complex permittivity (ε_r') is described as follows [236]:

$$\varepsilon_r' = \varepsilon_\infty - \frac{\omega_{pd}^2}{\omega^2 + \tau^{-2}} + \frac{\omega_{pl}^2(\omega_0^2 - \omega^2)}{(\omega_0^2 - \omega^2)^2 + \omega^2\gamma^2} \qquad (5.4)$$

where, ε_∞ is the permittivity extrapolated towards high frequency, ω_{pl} is the Lorentz angular plasma frequency, ω_0 is the resonance frequency, ω_{pd} is the Drude angular plasma frequency, which is related to carrier concentration (n_{eff}), effective mass (m^*) and, e is a charge of an electron (= 1.6×10^{-19} C)

$$\omega_{pd} = \sqrt{\frac{n_{eff}.e^2}{m^*.\varepsilon_0}} \qquad (5.5)$$

By considering the presence of both free and bound charge carriers in the synthesized samples, the Drude-Lorentz (DL) model was fitted to the experimental data points as shown in Fig. 5.4(b) for the SMS3 and SMS5 for the temperatures above the critical transition temperature (T_c). In Fig. 5.4(b) solid lines represent data generated according to the Drude-Lorentz model (Eqn. (5.4)) and symbols to the experimental data points. The ε_r' vs log f curves at different temperatures are in good agreement with the Drude-Lorentz model which confirms the presence of both free and bound charge carriers in both the samples up to the highest temperature of the measurement i.e., up to 600 ^oC. Absence of resonance characteristics in the experimental data and theoretically calculated according to Eqn. (5.4) can be due to dominating response of the plasmonic oscillations of free electrons over the resonance response of localized

charges. A decreasing trend of the absolute value of negative permittivity with increasing frequency is according to the Drude model.

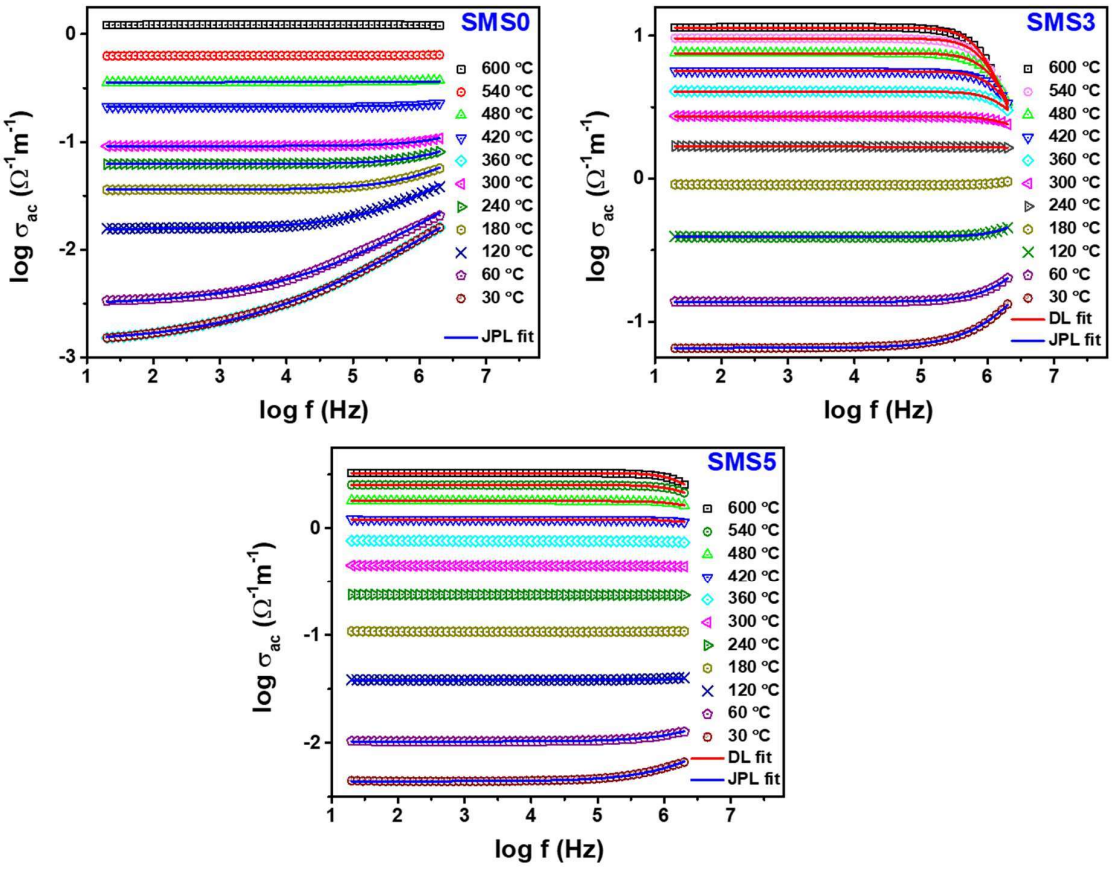

Figure 5.5. AC conductivity spectra of the samples at some representative temperatures.

The observed negative permittivity can be correlated with ac conductivity (σ_{ac}). Fig. 5.5 shows the frequency dependences of ac conductivity at few selected temperatures for all the samples. The ac conductivity (σ_{ac}) remains constant up to a certain frequency and above that it depends on the frequency. In Fig. 5.5, symbols are experimentally measured data points and solid lines represent fitting according to two different theoretical models discussed below. It's observed that for the temperatures below critical transition temperature (T_c), σ_{ac} is almost frequency independent up to a certain frequency (called hopping frequency, ω_h), above this frequency, σ_{ac} increases with the frequency (Fig. 5.5). The incremental part of the conductivity can be explained by employing Jonscher's power according to below [238]:

$$\sigma_{ac} = \sigma_{dc} + A\omega^n \qquad (5.6)$$

where σ_{dc} is direct conductivity, ω is the angular frequency, A is the preexponential factor and n is the frequency exponent that lies between $0 < n < 1$. A good fitting of Jonscher's power Law (Eqn. (5.6)) to experimental data points of the conductivity for temperatures below the critical temperature (T_c) indicates that the conduction mechanism is mainly via hopping of charge carriers that are localized (bounded) at defects. The hopping conduction mechanism has been reported in the systems in same ions are present in two different valence states [179].

For the temperatures above critical transition temperature (T_c), the decreasing part of the conductivity showed the metal-like conduction behavior (skin effect of the conduction electrons) in the samples. The Drude-Lorentz oscillator model was used to account for the high temperatures (above T_c) ac conduction behavior of the samples. According to this model, conductivity is related to various parameters as shown in the Eqn. (5.7) [236]:

$$\sigma_{ac} = \frac{\sigma_{dc}}{1+\omega^2\tau^2} + \frac{\varepsilon_0\omega_{pl}^2\omega^2\gamma}{(\omega_0^2-\omega^2)^2+\omega^2\gamma^2} \qquad (5.7)$$

where, σ_{dc} is the dc limit of Drude conductivity, τ is the average scattering time of carriers, ω_{pl} is the Lorentz angular plasma frequency, ω_0 is the resonance frequency, and γ is the damping factor. The first part of Eqn. (5.7) represents the contribution of free electrons, while the second part to the resonance response of localized/bound electrons. A good matching between measured data and data calculated according to Eqn. (5.7) is an evidence of dominating role of the free charge carriers with increasing temperature.

The observed change in the conduction mechanism in the samples is explained as follows. In the prepared samples Mn and Sn ions are present, these ions may be present in mixed-valence. The probable valence states for Mn ion are Mn^{3+} and Mn^{4+} whereas for Sn ions they are Sn^{2+} and Sn^{4+}. Mn^{3+} ion with an electronic configuration of $3d\ t_{2g}^3 e_g^1$ have an

additional electron in e_g orbital than Mn^{4+} ion with electronic configuration $3d\ t_{2g}^3 e_g^0$. Similarly, Sn^{2+} ion with electronic configuration $4d^{10}\ 5s^2\ 4p^0$ have two additional electrons than Sn^{4+} ions with electronic configuration $4d^{10}\ 5s^0\ 4p^0$. The additional $3d\ e_g$ electrons of Mn^{3+} ions and $5s^2$ electrons of Sn^{2+} ions locally transferred to their higher valent state (Mn^{4+}/Sn^{4+}) through an oxygen atom and contribute to the ac conductivity, σ_{ac} by hopping mechanism [263–265]. At high temperatures (above T_c) electrons localized at Mn^{3+} and Sn^{2+} get delocalized by thermal excitation processes to the edge of the conduction band, behave as free charge carriers. These free charge carriers will govern the ac conduction mechanism as observed in the metals (skin effect, decrease in the conductivity with increasing frequency according to the Drude model).

The variation of DC conductivity, at few representative temperatures with dopant concentration is shown in Fig. 5.6. It is noted from Fig. 5.6 that the DC conductivity of all the samples decreases with increasing temperature, which ensures the semiconducting nature of the samples even up to 600 ^oC. Furthermore, the conductivity of the sample is in the order SMS3 > SMS5 > SMS0. It is important to mention here that the temperature at which permittivity changes sign i.e., critical temperature (T_c) is in reverse order i.e., T_c of SMS0 > SMS5>SMS3. It means that critical temperature (T_c) is inversely proportional to dc conductivity, σ_{dc}. The DC conductivity, $\sigma_{dc}(= ne^2\tau/m$, where n - charge carrier density, e-electronic charge, τ - the mean collision time and m -the effective mass of the electron) is directly proportional to charge carrier density, and hence critical transition temperature (T_c) of Sr_2MnO_4 can be tuned by chemical doping.

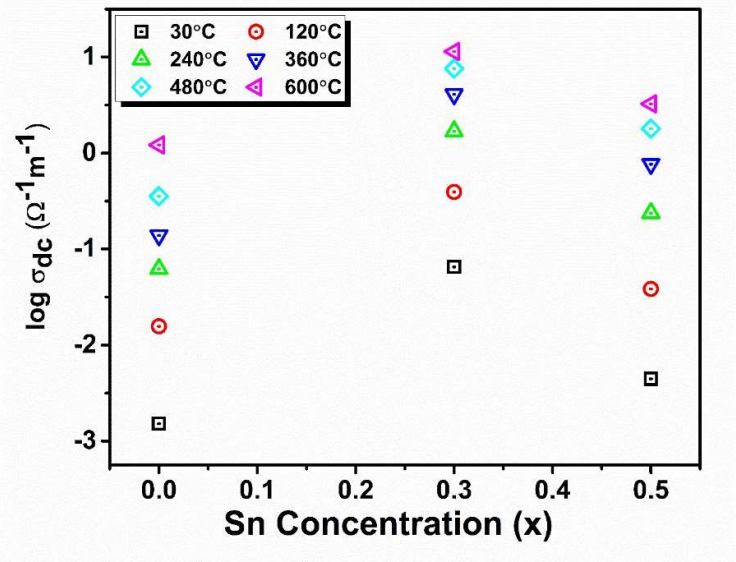

Figure 5.6. Variation of DC conductivity with increasing temperature and Sn Concentration (x).

In the solid solution $Sr_2Mn_{1-x}Sn_xO_4$, dopant Sn^{4+} and host Mn^{4+} have the same valences, and hence dopant-induced charge carriers are not expected. As mentioned above that Mn and Sn ions are multivalent, and exist in their lower valence state depending on the processing conditions and dopants. The presence of these ions other than the expected Mn^{4+} and Sn^{4+} states will produce defects and affect the value of conductivities (both σ_{dc} and σ_{ac}). It is worthy to mention here that these samples were synthesized at 1500 ^oC, and hence possibility of oxygen vacancies in the samples cannot be ruled out. X-ray photoelectron spectroscopy (XPS) has been used to elucidate the valence state of the constituent ions (Mn and Sn), results are discussed below.

5.3.4 XPS Analysis

Fig. 5.7 shows the Mn 2p and Sn 3d spectra of the samples SMS3 and SMS5. All binding energies were calibrated based on the C 1s peak at 285 eV. The spectrum of Mn exhibits two primary peaks for all the samples corresponding to Mn $2p_{1/2}$ and $2p_{3/2}$ due to spin-orbit coupling. The position of these peaks remains almost the same for all the samples. However,

the broadening and asymmetry of the peaks are different for different samples. The peak corresponding to Mn $2p_{3/2}$ was deconvoluted to investigate the possible valence states. The XPS core level binding energy corresponding to different elements and their valence states are summarized in Table 5.2. Their fraction (%) calculated from the peak area is also mentioned in Table 5.2.

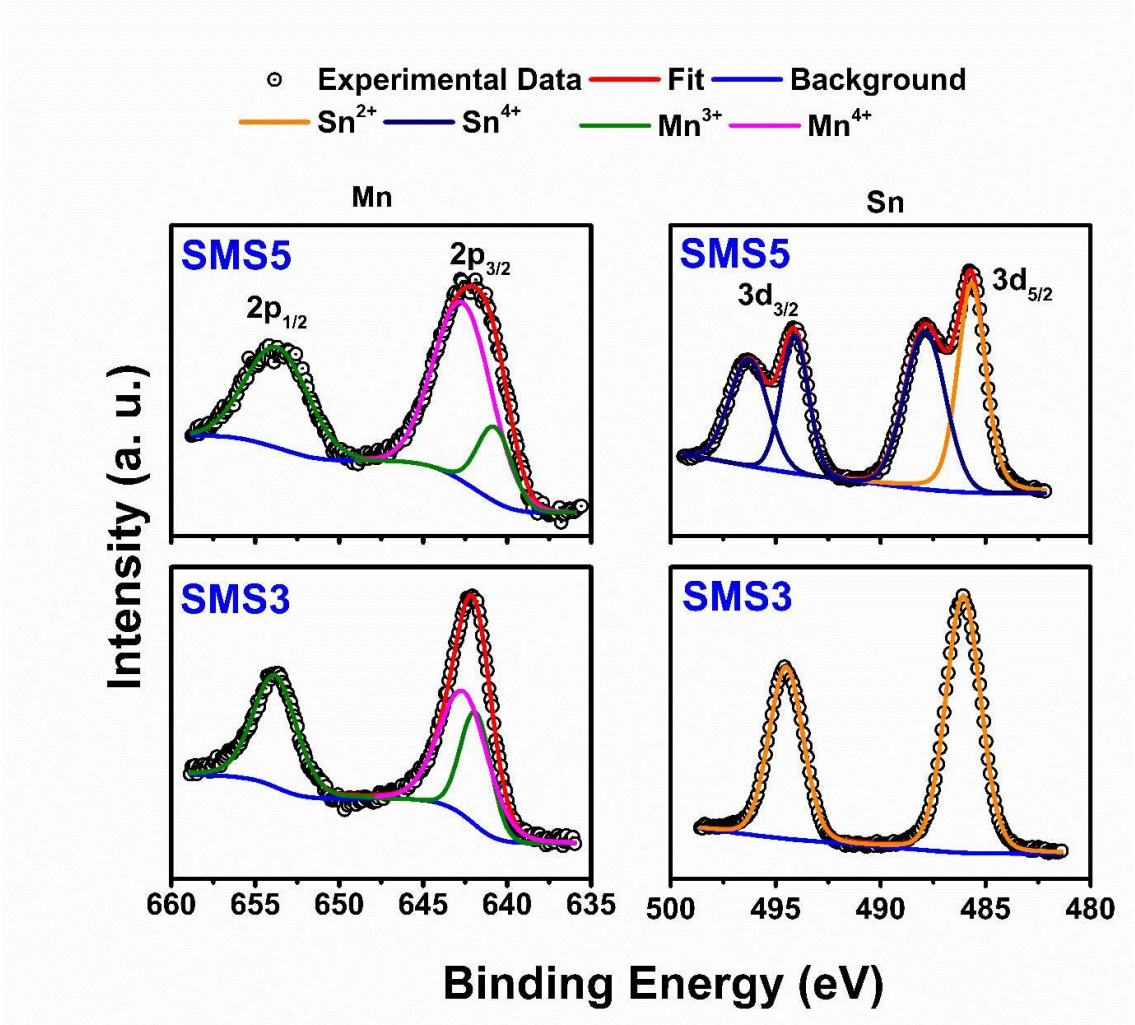

Figure 5.7. Core-level XPS spectra of Mn 2p and Sn 3d. Symbols represent the recoded spectrum and the solid line represents the fit and background.

The core spectra of Sn 3d for the samples SMS3 and SMS5 are also shown in Fig. 5.7. In sample SMS3 two peaks corresponding to Sn $3d_{5/2}$, Sn $3d_{3/2}$ were observed whereas, in the spectrum of the sample SMS5, four peaks were seen. The difference in the spectrum of Sn for

SMS3 and SMS5 suggests that in the sample SMS5, Sn ions are present in two different states while in the SMS3 sample they are present in only one state. The lower binding energy peaks are assigned to Sn^{2+} state and higher binding energy peaks to Sn^{4+} state of Sn ion. The exact value of binding energy of these ions is given in Table 5.2. It is already mentioned that these samples were prepared at 1500 °C, therefore loss of oxygen from the lattice is expected. According to defect chemistry, the loss of oxygen in Kröger–Vink notation is as follows:

$$O_o^{\times} \rightarrow V_o^{\bullet\bullet} + 2e' + \frac{1}{2}O_2(g) \uparrow \qquad (5.8)$$

The elections released in Eqn. (5.8) may be captured by Mn^{4+} and Sn^{4+} ions and reduce to Mn^{3+} and Sn^{2+}, respectively. In the literature, it has been mentioned that the Sr_2MnO_4 phase can be stabilized at lower temperatures only when it contains around 30% Mn ions into Mn^{3+} state. Reduction of Mn^{4+} state in Mn^{3+} state has been realized by synthesizing in reducing atmospheres and quenching [238]. As the samples SMS3 and SMS5 in this work were prepared by normal cooling (4 °C/min.), thus to stabilize Sr_2MnO_4 phase an optimum number of Sn^{4+} ions have to reduce to Sn^{2+} ions. In the sample SMS3 concentration of Sn is 30 mol% whereas in SMS5 it is 50 %, thus it is possible that in sample SMS all Sn ions are present in Sn^{2+} while in SMS5, Sn^{4+} ions are present in both Sn^{2+} and Sn^{4+} states. The Mn^{3+} and Sn^{2+} ions in the lattice of Sr_2MnO_4 are treated as defects and will create their energy level in the bandgap. The sum of % of Mn^{3+} and Sn^{2+} is in the order SMS3>SMS5>SMS0 same as we have observed for the dc conductivity, σ_{dc}. The UV-Vis.-IR spectroscopy technique was employed to provide experimental evidence for existence of the highest number of defects in the sample SMS3. The results of UV-Vis-IR spectroscopy have been analyzed and discussed below.

Table 5.2. XPS core level binding energy of Mn 2p and Sn 3d.

Sample Code		SMS3		SMS5	
Elements		B. E. (eV)	Concentration (%)	B. E. (eV)	Concentration (%)
Mn $2p_{1/2}$		653.9	30 % in Mn^{3+} and 70 % in Mn^{4+}	653.8	20 % in Mn^{3+} and 80 % in Mn^{4+}
Mn $2p_{3/2}$	Mn^{3+}	641.8		641.2	
	Mn^{4+}	642.7		642.4	
Sn $3d_{3/2}$	Sn^{2+}	494.4	100 % in Sn^{2+}	494.1	50 % in Sn^{2+} and 50% Sn^{4+}
	Sn^{4+}	-		496.4	
Sn $3d_{5/2}$	Sn^{2+}	486.0		485.6	
	Sn^{4+}	-		487.9	

5.3.5 UV-Vis-NIR Spectroscopy

The UV-Visible-Near Infra-Red (UV-Vis.-NIR) spectrum of the samples SMS3 and SMS5 was recorded in the wavelength range of 300-1700 nm. The absorption spectrum of the samples SMS3 and SMS5 are shown in Fig. 5.8. For comparison, the UV-Vis.-IR spectrum of the sample SMS0 taken from the reference [238] is also shown in Fig. 5.8. In the spectrum of sample SMS3 about 90% (higher absorbance) in the entire Vis.-IR region is seen. The absorbance in the samples is in the order SMS3 > SMS5 > SMS0, was observed. The high absorbance in SMS3 and SMS5 implied a continuum states/bands in the forbidden bandgap region due to quantum mechanical penetration of the localized states corresponding to defects. The reduction of Mn and Sn ions generates defect centers in the crystal due to mismatch in ionic radius as well as charge compensation mechanism. The defects introduce a strong

potential gradient in the host matrix, which causes the quantum mechanical penetration of the localized states into the forbidden band-gap.

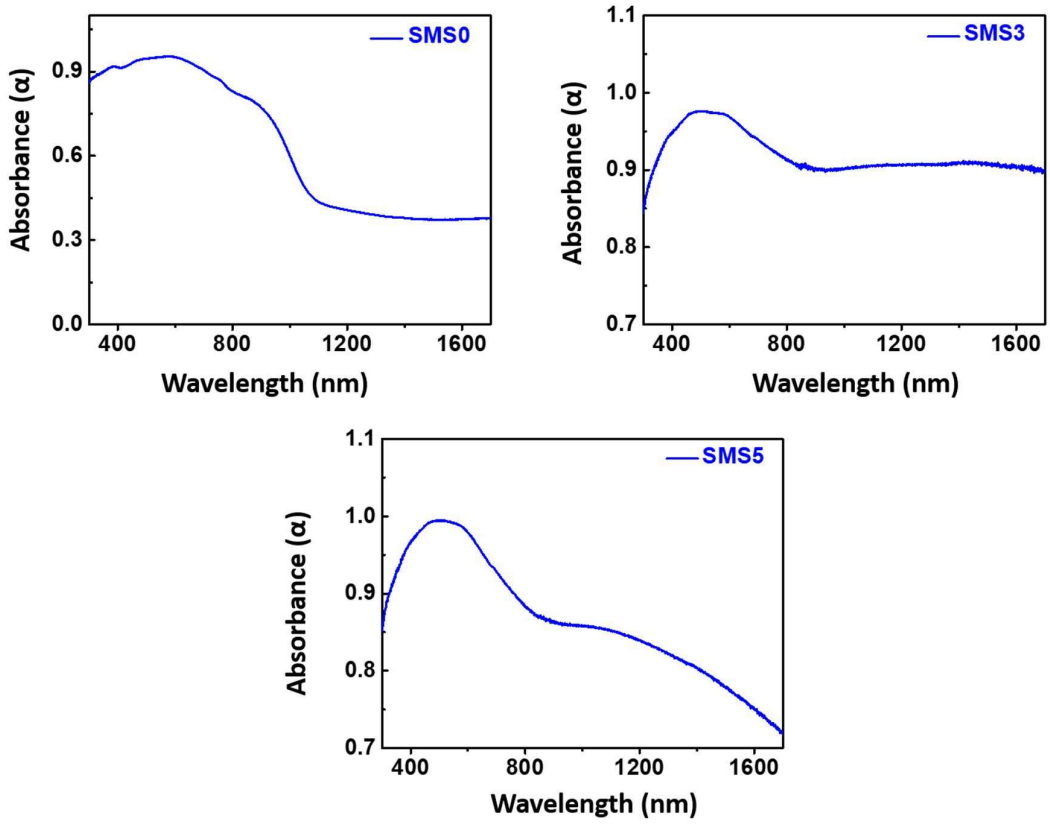

Figure 5.8. UV-Vis-IR absorption spectra of the samples.

On careful observation of the spectra, it is found that absorption peak shift towards lower wavelength side on increasing Sn concentration (x) indicating a widening of the band. Widening of the band is possible on substitution of Sn at Mn site of Sr_2MnO_4 because bandgap of estimated by Tauc's plot for Sr_2MnO_4 is 1.15 eV [238] while for Sr_2SnO_4 is 4.20 eV [266].

The XPS and UV-Vis.-IR spectroscopy results (discussed above) have shown that the density of defects for the sample SMS3 is higher than that of the Sr_2MnO_4 (SMS0) and for the sample SMS5 is between them. As we know from the band theory, the higher defect density in the forbidden bandgap region enables the thermal excitation of carriers at a lower temperature. Therefore, threshold carrier concentration or critical transition temperature (T_c) for achieving

negative dielectric permittivity is lowest (~220 °C) for the sample SMS3 and highest (~580 °C) for the sample SMS0.

5.4 Conclusions

Single-phase powder and ceramic of layered oxides $Sr_2Mn_{0.70}Sn_{0.30}O_4$, $Sr_2Mn_{0.50}Sn_{0.50}O_4$, $Sr_2Mn_{0.30}Sn_{0.70}O_4$ and Sr_2SnO_4 were successfully synthesized. Rietveld refinement confirmed tetragonal structure and space group I4/mmm same as of the Sr_2MnO_4. SEM images analysis has indicated a change in the grain's morphologies on Sn substitution. A change over from positive to negative in permittivity is observed in Sr_2MnO_4, $Sr_2Mn_{0.70}Sn_{0.30}O_4$ and $Sr_2Mn_{0.50}Sn_{0.50}O_4$ compositions. The negative permittivity behavior in the frequency range 1kHz-2 MHz is attributed to plasmonic oscillations of free carriers, generated by the thermal excitation process. Study of ac conductivity (σ_{ac}) has indicated a change in the conduction behavior from hopping to metal-like (skin effect) with increasing temperature. A good matching between experimental data and the Drude-Lorentz model of permittivity and ac conductivity (σ_{ac}) confirmed the presence of both localized and free charge carriers in the samples. XPS analysis has confirmed the presence of both Mn and Sn ions in mixed-valence states Mn^{3+} - Mn^{4+} and Sn^{2+} - Sn^{4+}, respectively. Lastly, it is concluded that the negative permittivity behavior of Sr_2MnO_4 can be tuned by selecting suitable dopants for the Mn site.